Microstructure and Wear Resistance of a Ni–Fe–Si–B Amorphous Composite Coating by Laser Cladding

Xuanhong Hao[1] · Hongxi Liu[1] · Xiaowei Zhang[1] · Yueyi Wang[1] · Chen Yang[1] · Yaxia Liu[1]

Abstract

In this study, a Ni–Fe–Si–B amorphous composite coating is coated on H13 steel by laser cladding. Coatings are systematically investigated for their microstructure, phase composition, tribological behavior, and mechanical characteristics. X-ray diffraction results demonstrate that the cladding layer can be divided into the interface, transition, and compositionally stable zones, where the coating has both crystalline and amorphous phases, with up to 57% of the coating being amorphous. According to scanning electron microscopy and transmission electron microscopy analyses, the middle and surface regions of the coating mainly consist of $(Fe_{0.5}Ni_{0.5})_3Si$, Fe_2B, Fe_2NiB, $Ni_{31}Si_{12}$, and amorphous phases. The in-situ generated Fe_2B phase is uniformly distributed within the coating, leading to a significant enhancement in microhardness. The greatest hardness of the coating is approximately 927.04 $HV_{0.2}$. The composite coating exhibits excellent wear resistance, which is approximately 1.71 times greater than that of the substrate. Minor abrasive wear constitutes the primary wear mechanism for the coatings.

1 Introduction

Due to their superior surface qualities, such as high microhardness and resistance to wear, corrosion, and oxidation, amorphous alloys have been extensively utilized in surface coatings [1–8]. Laser cladding, a sophisticated surface modification process, is distinguished by its great precision and quick heating and cooling speeds. In laser processing, the cooling rate may reach up to 108 K/s, and fast, non-equilibrium cooling can be achieved, which is favourable to the creation of a glassy phase. Therefore, laser cladding has been utilized to manufacture amorphous metal coatings with little or no crystallization [9–12].

Utilizing laser-cladding technology, significant attempts have been undertaken to produce amorphous coatings throughout the years. Because of their exceptional mechanical and physical properties, such as high yield strength, excellent soft magnetic properties, high thermal stability, and high corrosion resistance, as well as their abundant natural resources and low material costs, Fe-based, Ni-based, and Fe-Ni based bulk glassy alloys (BGAs) are of particular interest among metal-based BGAs [13–15]. To prevent fracture development during laser cladding of a $Fe_{37.5}Cr_{27.5}C_{12}B_{13}Mo_{10}$ amorphous coating, Lu et al. [16] used a triple laser scanning method to relieve the thermal tension created inside the amorphous coating in situ. Shu et al. [17] used the laser-cladding method to fabricate CoCrBFeNiSi high-entropy alloy coatings. This could be separated into three layers with distinct microstructures, including a dendritic layer, an amorphous layer, and a transition layer. Chang et al. [18] wanted to produce a Ni–Cr–Si–B–Fe amorphous ribbon coated on a substrate of mild steel using laser additive manufacturing. The X-ray diffraction (XRD) findings revealed that amorphous and crystalline phases coexisted in the coating, with the amorphous phase constituting up to 41% of the coating. Zhang et al. [19] used the laser-cladding method to fabricate amorphous and crystalline Fe–Ni–B–Si–Nb composite coatings and improved the abrasion resistance of the coatings in amorphous phases. The coatings

✉ Hongxi Liu
kustliuhx@sina.com

✉ Xiaowei Zhang
amkust@kust.edu.cn

1   The Faculty of Materials Science and Engineering, Kunming University of Science and Technology, Kunming 650093, China

exhibited performance superior to that of the substrate. By forming the NiO passivation film by adding Ni, Kong et al. [20] evaluated the effects of Ni addition on the immersion corrosion and described the electrochemical corrosion behaviors of FeSiBNi coatings in 3.5% NaCl solution. This significantly increased the corrosion resistance of FeSiBNi coatings.

It has been shown that FeNi-based amorphous alloys exhibit exceptional characteristics when utilized as coatings. Nevertheless, the challenge lies in effectively managing the dilution rate of the coating during laser cladding in real-world operational settings. This process is further complicated by the diffusion of elements from the matrix, which alters the composition of the intended coating. It is widely acknowledged that amorphous alloys exhibit a high sensitivity to variations in alloy compositions. Consequently, when employing laser cladding, the typical outcome is the production of amorphous composite coatings. Previous research has primarily concentrated on enhancing the amorphous characteristics of the coating. In contrast, the present study aims to investigate the formation process of intricate tissue phases within composite coatings. This work involved the laser cladding of a Ni-Fe-Si-B amorphous composite coating and involved a thorough analysis of the cross-section morphologies, element distribution, and surface phase of the cladding layer. In order to identify the processes governing the evolution of microstructure, the microstructure and phase distribution of the amorphous composite coating were examined. Then, the cladding layer's microhardness and wear resistance were assessed and contrasted with those of the H13 steel substrate.

2 Experiment

2.1 Materials and Methods

The $Ni_{40}Fe_{32}Si_{12}B_{16}$ alloy powders were chosen as the cladding materials for this experiment. The substrate used was an H13 steel plate with dimensions of 50 mm × 10 mm × 5 mm. To prepare the substrate, it was sanded with 200#, 400#, and 600# sandpapers to remove any residual oil stains and oxides, which could interfere with the laser cladding process. The sanding also helped reduce the reflection of the laser. Once sanded, the substrate was further cleaned by ultrasonically immersing it in acetone and ethanol. The powders used in the experiment were obtained from Changsha Tianjiu Metal Materials Co., LTD, China. The Fe, Ni, and Si powders used had a purity of 99.9%. To ensure that there was no excessive burning of B, boron was added in the form of boron iron powder. In addition, any insufficient Fe was supplemented with Fe powder. The powders were then mixed in a planetary ball grinding mill for 3 h at a ball-to-powder mass ratio of 4:1 and a speed of 200 r/min. Once the powders were properly mixed, they were combined with 96% alloy powder and 4% absolute ethanol based on the mass fraction. This mixture resulted in a viscous alloy powder. The alloy powder was then evenly pressed onto the surface of the H13 steel substrate. The dimensions of the preset layer were 50 mm × 3 mm × 1 mm. For the laser cladding process, a 6 kW multimode constant current CO_2 laser with the model number GS-TEL-6000 A was used as the light source. The laser scanning speed was set at 400 mm min − 1, and the laser power was set at 4 kW. To prevent oxidation during the deposition phase, the entire laser cladding procedure was protected by an argon environment with less than 10 ppm of oxygen and moisture. A coaxial nozzle was used to spray pure argon gas at a flow rate of $20 \ L \cdot min^{-1}$ to serve as the protective gas. The argon gas used had a purity of 99.99%.

2.2 Characterization

Different regions of the coating were tested using micro-area XRD diffraction. The phase of the coating was determined using an Empyrean X-ray diffractometer. The microstructure was examined with a TESCAN VEGA3 scanning electron microscope (SEM), and the coating was analyzed using energy-dispersive X-ray spectroscopy (EDS) with OXFORD spectroscopy. A slice was cut using the Helios G4 PFIB HXe focused ion beam (FIB) equipment. Further characterization of the microstructure and crystal structure of the SLMed specimens was conducted using a transmission electron microscope (JEM-F200, JEOL, Japan) equipped with an energy-dispersive X-ray spectroscope (JED-2300T, Japan) system. To accurately determine the distribution of boron in the coating structure, electron probe microanalysis (EPMA) was performed on Ni-Fe-Si-B composite coating samples using an AHIMADZU EPMA-1720 microanalyzer. The microhardness of the cross-sectional region of the composite coatings was assessed using a Micro Vickers Hardness Meter from the HMV-GFA series. Esteemed measures were taken to ensure consistency, including 20 points being measured, a loading load of 1.961 N, and a loading time of 10 s. The wear resistance of the coatings was evaluated using a versatile abrasion-testing device (UMT-2) with balls made of Al_2O_3. The wear tests were conducted using the reciprocating wear technique, with testing conditions including a 20 N load force, a 1.5 mm wear scar length, a 1 Hz swing frequency, and a 30 min wear time. The three-dimensional (3D) shape of the wear trace was obtained using a 3D profilometer (Model: Micro XAM-800). By analyzing the wear traces collected using SEM, the wear mechanism of the coating was identified.

3 Results and Discussion

3.1 Microstructure of Ni–Fe–Si–B Coating

Figure 1 shows the cross-sectional morphologies of the Ni–Fe–Si–B composite coating and the H13 steel. There is a distinct bright band between the coating and the substrate, which is a distinctive feature of laser-cladded coatings. This behavior suggests that during the cooling and solidification of the molten pool, the melted substrate surface layer and the cladding powder become miscible and diffuse, resulting in a good and tight metallurgical bond between both of them. The organization of the coating solidifies in a manner that transitions from planar crystal growth to cellular crystal growth and then to dendrite growth. The microstructure revealed that the coatings were made up of three layers; a compositionally stable area at the top of the coating, a middle transition area, and an interface area at the bottom. To determine the phase structure of the different regions, micro-XRD analysis was performed on the three coating regions.

Figure 2 illustrates the XRD pattern of the Ni–Fe–Si–B composite coating. It can be observed that the XRD of different regions is different. Figure 2A illustrates the XRD pattern of the top surface of the cladded coating. The crystalline peaks were identified as $(Fe_{0.5}Ni_{0.5})_3Si$, Fe_2B, and $Ni_{31}Si_{12}$. In the middle area of the coating (Fig. 2B), the diffraction peaks are broadened between $2\Phi = 43–45°$, and there is a clear diffusion scattering peak, which is one of the typical characteristics of amorphous coatings [21, 22]. There are strong crystal diffraction peaks superimposed on the scattering peak, indicating that the middle area of the coating is the coexistence of amorphous and crystalline phases. This also shows that the structure in the middle region of the coating that shows no grain boundary features in Fig. 1 is mainly a composite structure of amorphous and crystalline phases. The Pseudo-Voigt function was used to fit the XRD pattern in the middle region of the coating using the Verdon method. The amorphous content was 57%. The planar crystal region of the coating and the substrate (Fig. 2C) is the superposition of three peaks, and analyses show that it is the superposition peak of $(Fe_{0.5}Ni_{0.5})_3Si$, Fe_2B, and α-Fe. Combined with the rapid solidification process of laser cladding, the micro-area XRD results of the above coatings in different areas are analyzed. In the laser-cladding process, part of the H13 steel matrix surface melts due to laser heating, which results in a significant dilution of the Fe element in the matrix, As a result, the organization of the coating is somewhat non-uniform, and various regions of the coating cross-section exhibit distinct properties; this is primarily due to the presence of a temperature gradient in the coating throughout the laser processing [17, 23, 24]. According to the composition distribution, the cladding layer can be divided into interface, transition, and compositionally stable zones. During the formation of the coating, the difference in the cooling rate results in significant variance in the XRD results between the different regions. And due to the difference in temperature gradient, the temperature

Fig. 1 (**a**) Cross-sectional morphologies of the Ni–Fe–Si–B composite coating; (**a1**) Macro morphology of composite coating; Macrograph of coating cross-section: (**b**) A compositionally stable area at the top of the coating, (**c**) a middle transition area, and (**d**) an interface area at the bottom
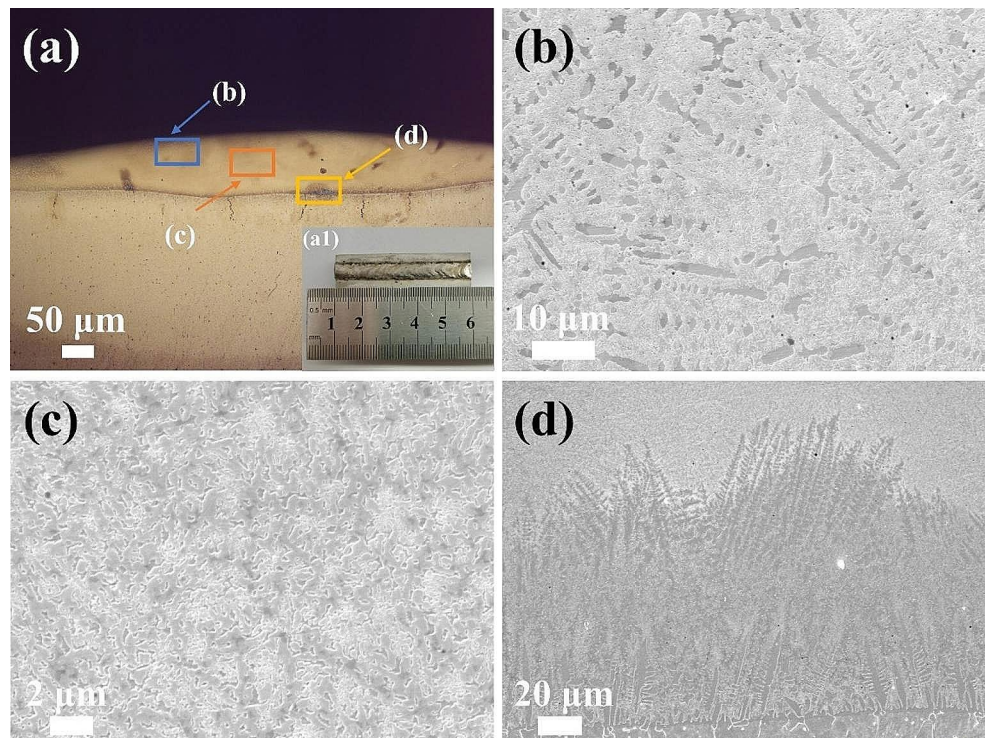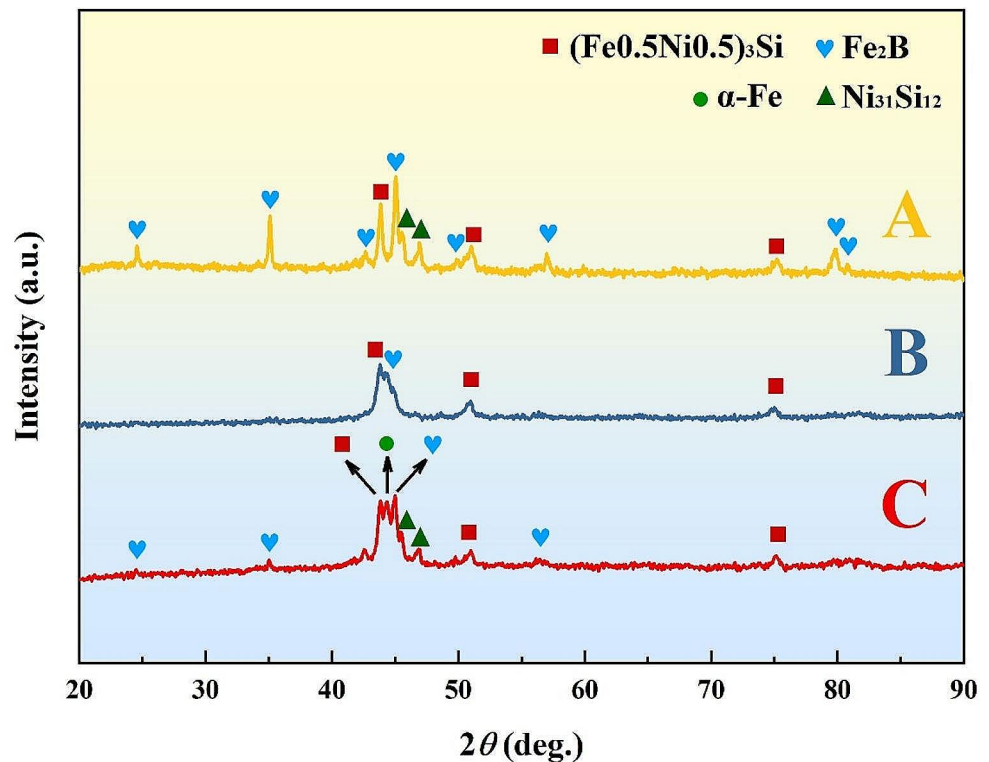
Fig. 2 XRD patterns of Ni–Fe–Si–B coatings; A compositionally stable area (**A**) at the top of the coating, a middle transition area (**B**), and an interface area (**C**) at the bottom

gradient in the composition stabilization zone (top of the coating) is the smallest, the solidification rate is the largest, and the amorphous phase disappears. The organization in the composition stable zone (top of the coating) is mainly $(Fe_{0.5}Ni_{0.5})_3Si$, Fe_2B and $Ni_{31}Si_{12}$ phases. In contrast, significant α-Fe phase precipitation can be seen in the interfacial region (bottom of the coating), mainly due to the largest temperature gradient, while the molten pool is subjected to dilution by Fe elements from the matrix. Elemental diffusion between the matrix and the coating disturbed the elemental composition of the coating in this region, and therefore no amorphous organization was generated. The organization in the interfacial zone (bottom of the coating) is dominated by $(Fe_{0.5}Ni_{0.5})_3Si$, Fe_2B and α-Fe phases.

Owing to the small atomic number of B, it is difficult to accurately detect its content using an energy spectrometer. The microstructure and energy spectra of different regions were obtained using an electron probe EPMA (Fig. 3). (Fig. 3(a)) forms dendrites dominated by Fe, Ni, and Si, whereas B is mainly concentrated in the intergranular region. In the transition zone of coating (Fig. 3(b)), the distribution of elements is uniform, and the stable composition of coating. It can be observed that the interface area of the coating (Fig. 3(c)) due to the dilution of the H13 steel matrix by laser cladding, the Fe element is greatly diluted from the matrix into the coating to form α-Fe, a solid solution containing Ni, Fe, Si, NiSi phase, and Fe_2B. The cooling rate and composition of a particular metallic alloy system are

key elements in determining the amorphous microstructure [1]. Owing to the different cooling rates and molten pool flow fields in each area of the cladding layer, the microstructure also exhibits clear variances. According to the interface stability theory, the growth morphology of solidified tissue is mainly controlled by the temperature gradient and solidification rate (G/R) [10]. At the connection between the solution and the substrate (interface region), the temperature gradient G is the highest, and the solidification rate is the smallest; thus, G/R is the largest, and the solidified structure grows in a low-speed plane, forming a plane crystal based on α-Fe. With the growth of the planar crystal, the composition of the front of the planar crystal changes, and compositional supercooling occurs. Further, G/R decreases, the interface becomes unstable, and dendrites grow along the direction of maximum heat flow. With the growth of dendrites, G/R decreases further, and the dendrites are gradually refined until they are interrupted. As shown in Fig. 3, the molten pool formed a stable composite structure of amorphous and crystalline phases. On the upper part of the coating, owing to the small temperature gradient in this area and the influence of convective agitation in the molten pool flow field [25], the molten pool exhibited no clear heat dissipation direction, and dendrites with no clear heat dissipation direction were formed.

Analysis of the composite structure of the crystalline and amorphous phases in the transition zone in the middle of the coating is relatively complicated. To further analyze and
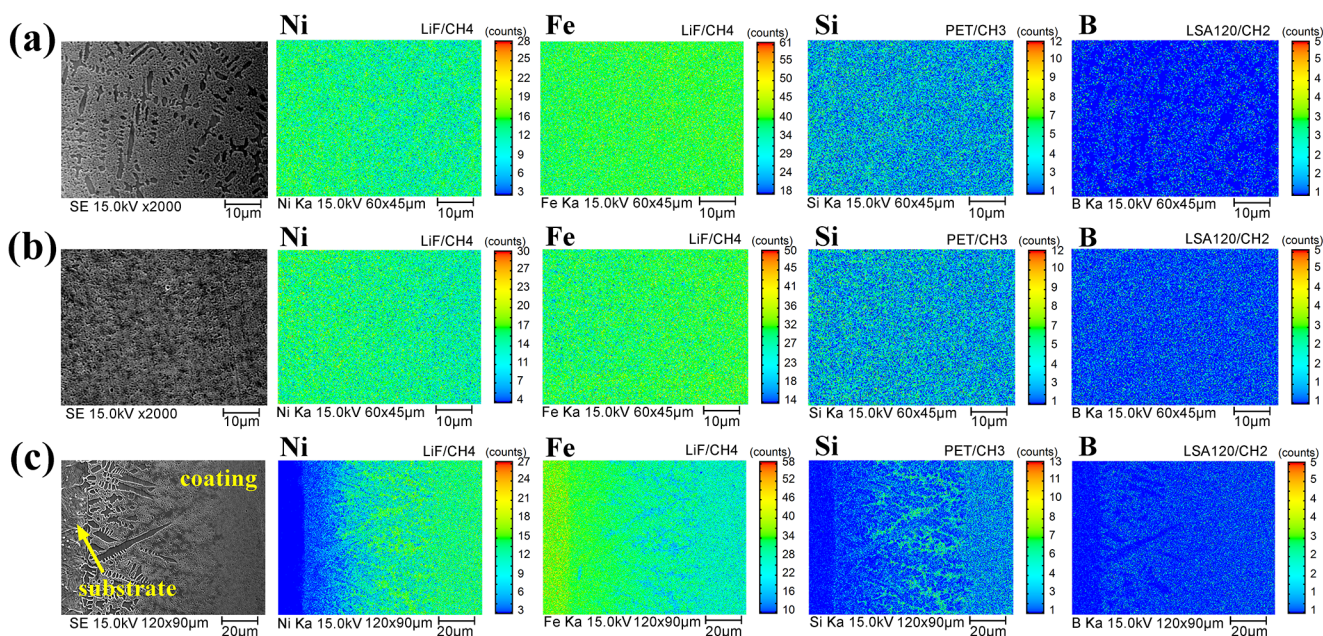
Fig. 3 Electron probe microanalysis of the Ni–Fe–Si–B coating; (**a**) compositionally stable zone, (**b**) transition zone, and (**c**) the interface zone

discuss the structure and growth process of each phase in the transition zone in the middle of the coating, the transition zone was cut using a FIB and characterized through high-resolution TEM. Figure 4 displays the acquired bright-field picture and a chosen area electron diffraction. The positions of the test points and results are listed in Table 1. According to the bright-field image (Fig. 4a) and the calibration results of the SAED spot obtained through electron diffraction of the selected area (Fig. 4b and e), region (b) was confirmed to be $(Fe_{0.5}Ni_{0.5})_3Si$, and its crystal band axis was [010]; area (c) was confirmed as the Fe_2B phase, and its crystal band axis was [$\bar{1}$13]; area (d) was confirmed as the Fe_2NiB phase, and its crystal band axis was [010]; area (e) was confirmed as the $Ni_{31}Si_{12}$ phase, and its crystal band axis was [$\bar{1}$21]; and, the blue area (f) represents the matrix in the upper right corner of the bright-field image. As shown in Fig. 4f, the blue area (f) is a partially amorphous region in the transition region, and nanocrystals are formed in the amorphous region. Lattice fringes corresponding to the (200) crystal plane can be observed at the edge. The results calculated using the integrated intensity demonstrate that the interplanar spacing of the (200) plane was 0.1783 nm, which is a slight increase compared to the interplanar spacing in the standard structure. This may be caused by the substantial amount of solid solution of Si in the Ni–Fe austenite. As shown in Fig. 4(g), the fast Fourier transform (FFT) of the amorphous region exhibits a diffuse scattering ring, further proving the existence of an amorphous phase in the transition region. The inverse FFT of the nanocrystal region was performed, as shown in Fig. 4h, and the presence of a small number of dislocations in the nanocrystal can be observed

from the obtained image. As shown in the bright-field images illustrated in Fig. 4(i) and 4(j), precipitation of the nanocrystalline Fe_2B phase was also observed. Therefore, we demonstrated that Fe_2B has two main forms: an elongated Fe_2B phase and a spherical nano Fe_2B phase.

The HAADF-STEM morphology and TEM-EDS chemical elemental composition distribution corresponding to the bright-field TEM image of the coating microstructural features in the above figure are shown in Fig. 5. In order for crystallization to start, an amorphous phase must typically supercool (meaning that the liquid state may be maintained without crystallization happening at temperatures much below the melting point). This is due to the fact that solid nuclei must first overcome an activation energy barrier, which is lower than the amount of undercooling [26]. In this study, a supersaturated solid solution of $(Fe_{0.5}Ni_{0.5})_3Si$ was formed first from the glassy phase. The solute (B and Si) atoms are rejected into the glassy phase because the concentration of the solute in the $(Fe_{0.5}Ni_{0.5})_3Si$ phase is lower than that in the glassy phase; as a result, the remaining glassy phase becomes enriched in B and Si until further crystallization is halted. Consequently, $(Fe_{0.5}Ni_{0.5})_3Si$ and the glassy phase with the altered composition are in a metastable equilibrium. Later, phases like $Ni_{31}Si_{12}$, α-Fe, and other crystalline phases may begin to crystallize. Combined with the aforementioned microstructural morphological characteristics and chemical composition analysis, it can be observed that during the solidification process of the molten pool, as the powder melts, the molten pool first forms an amorphous phase, and the solid-liquid front of the molten pool first precipitates to form Fe_2NiB owing to the supercooling of
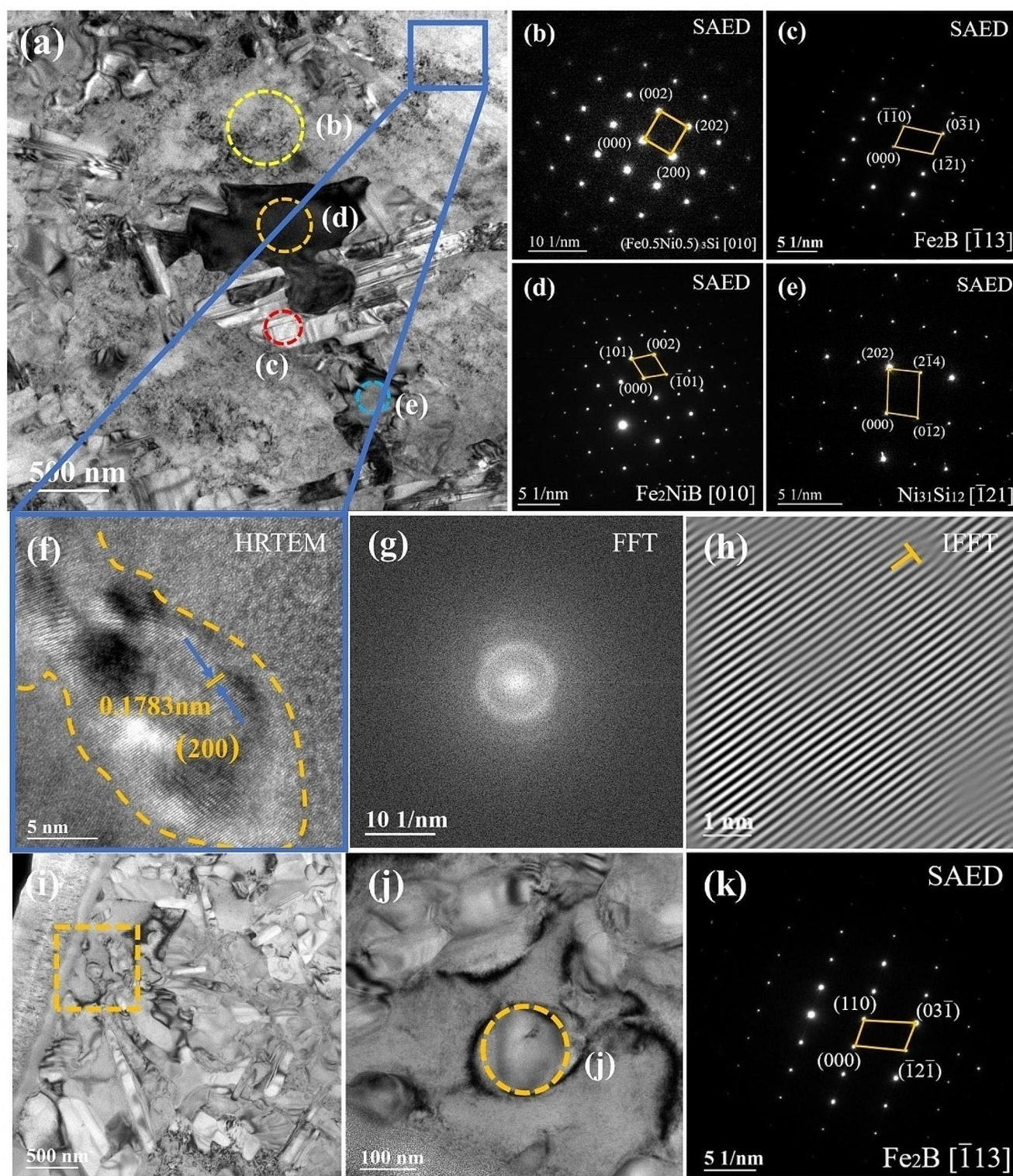
Fig. 4 Microstructural characteristics of the transition zone in the middle of the coating illustrated in Fig. 4: (**a**) bright-field TEM images; (**b–e**) diffraction patterns captured from the region labeled as SAED in (**a**); (**f**) HRTEM image of the blue area illustrated in (**a**) with corresponding (**g**) FFT and (**h**) IFFT images; (**i**) bright-field TEM images; and (**j**) bright-field TEM images of the nano-Fe_2B with corresponding (**k**) SAED images

Table 1 Test results of energy dispersive X-ray spectroscopy (EDS) points at different positions of the Ni–Fe–Si–B coating (at%)

Region	Phase	Element (at%)			
		Ni	Fe	Si	B
(b)	$(Fe_{0.5}Ni_{0.5})_3Si$	43.34	43.16	13.5	---
(c)	Fe_2B	5.93	68.07	0.07	25.93
(d)	Fe_2NiB	20.33	61.92	---	17.75
(e)	$Ni_{31}Si_{12}$	68.72	7.67	23.61	---
(j)	Fe_2B	9.25	60.79	---	29.96

the components. Owing to the Fe_2NiB phase, the remaining liquid phase precipitates and grows to form the Fe_2B phase, and finally, the remaining liquid phase forms the $Ni_{31}Si_{12}$ phase. Consequently, it is evident that the intricate arrangement of the coating is predominantly attributable to the substrate's dilution. The dilution rate markedly influences the formation and content of the amorphous phase in composite coatings during laser cladding. A fully crystallized matrix, abundant in nucleation centers, facilitates the transition of amorphous powder to crystallization during melting and solidification. Consequently, a higher dilution rate provides an increased number of crystallization sites, thereby potentially impeding the production of amorphous phases in composite coatings [27]. Which induces compositional changes within the coating and substantially diverges the organization composition from the nominal composition provided.

3.2 Mechanical Properties of the Ni–Fe–Si–B Coatings

The Fig. 6 shows the microhardness curves of coatings. the curve is divided into four parts: Compositionally stable zone, Transition zone, Interface zone and Heat affected zone. The bonding zone has an approximate hardness of 764.81 $HV_{0.2}$. the main reason for the low hardness in the interfacial zone is thought to be due to the drastic dilution between the H13 steel matrix and the melt pool, where the α-Fe phase, formed by the Fe elements from the matrix, is significantly lower compared to the high hardness of the $(Fe_{0.5}Ni_{0.5})_3Si$ and Fe_2B phases. The intermediate transition

zone exhibits a hardness of approximately 867.65 $HV_{0.2}$. This value can be primarily attributed to the composite coating's high hardness, which is composed of the amorphous, $(Fe_{0.5}Ni_{0.5})_3Si$, and Fe_2B phases. the $(Fe_{0.5}Ni_{0.5})_3Si$ phase has a very high hardness due to its unique topologically dense row structure with a very high coordination number and space utilization, which makes it difficult for dislocations and slips to nucleate [28]. The solid solution of the Si element in the FeNi phase has a clear effect of strengthening solid solutions, and some of the Fe_2B nanocrystalline phases that are diffusely dispersed efficiently increase the coating's hardness. The surface exhibits the greatest hardness, measuring approximately 927.04 $HV_{0.2}$. This phenomenon can be attributed to the deposition of a substantial quantity of the in-situ generated Fe_2B phase onto the coating surfaces. These Fe_2B phases possess exceptional abrasion resistance and hardness, thereby substantially enhancing the coatings' surface hardness.

3.3 Tribological Behavior of Ni–Fe–Si–B Coatings

Figure 7 shows the friction and wear results of the substrate and coatings. The coefficient of friction is a crucial indicator of the wear resistance of materials, and it reflects the surface morphology, contact form, and interaction between the load and sliding velocity. In general, the smaller the friction coefficient, the higher the wear resistance [29, 30]. As shown in Fig. 7(a), the coefficients of friction of the substrate and coating in the stabilization stage of frictional wear are about 0.7 and 0.4, respectively. As shown in Fig. 7(b), the wear volume loss of H13 was 12.25×10^4 μm^3, whereas that of the Ni–Fe–Si–B coatings was 7.16×10^4 μm^3.

According to Archard's wear law [31], the specific wear rate is defined as:

$$K = \frac{V}{N \cdot d} \tag{1}$$

where K denotes the specific wear rate, V is the wear volume (mm^3), N is the applied load (N), and d is the total sliding

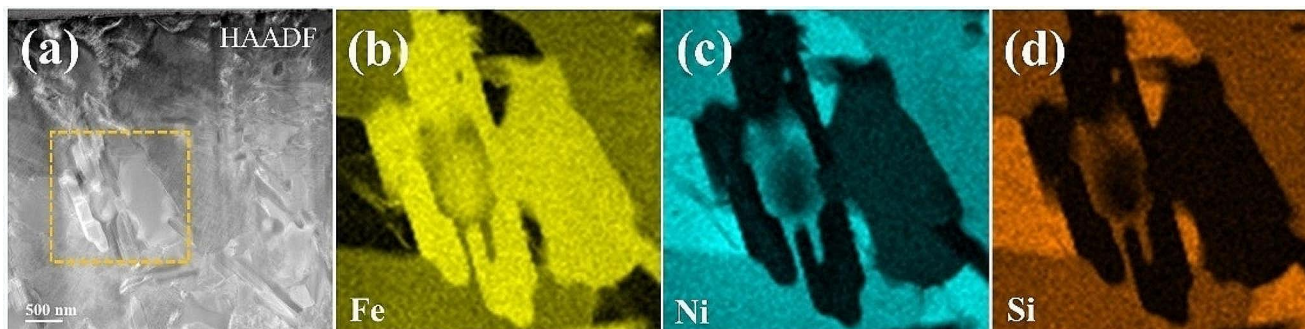**Fig. 5** TEM micrographs of microstructural characteristics of the Ni–Fe–Si–B coating: (**a**) bright-field TEM images; (**b**) HAADF-STEM micrograph with (**b**)–(**d**) corresponding elemental TEM-EDS maps

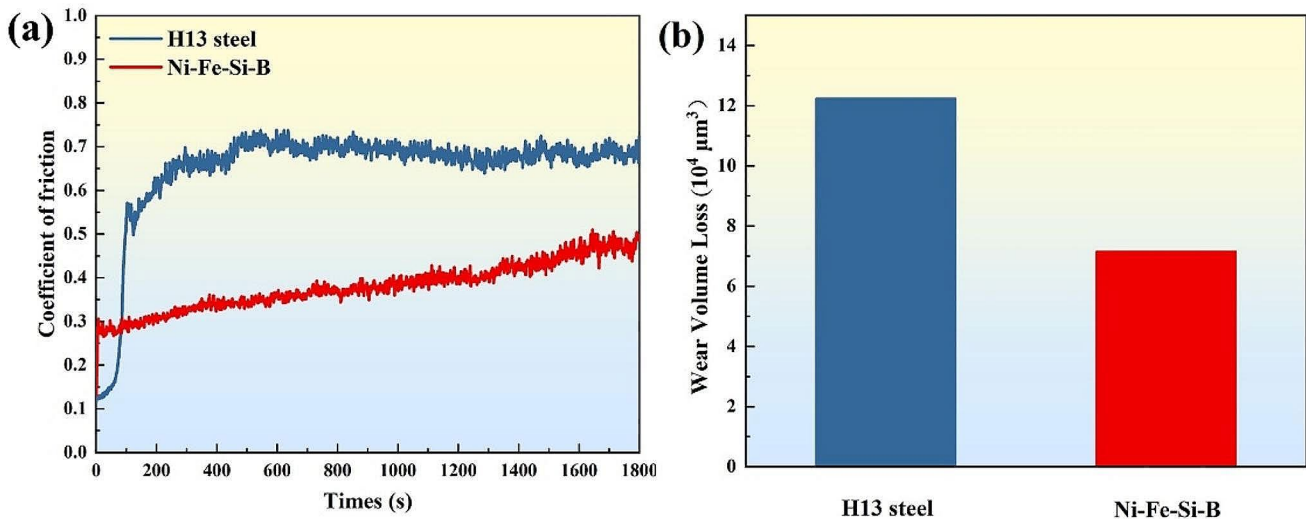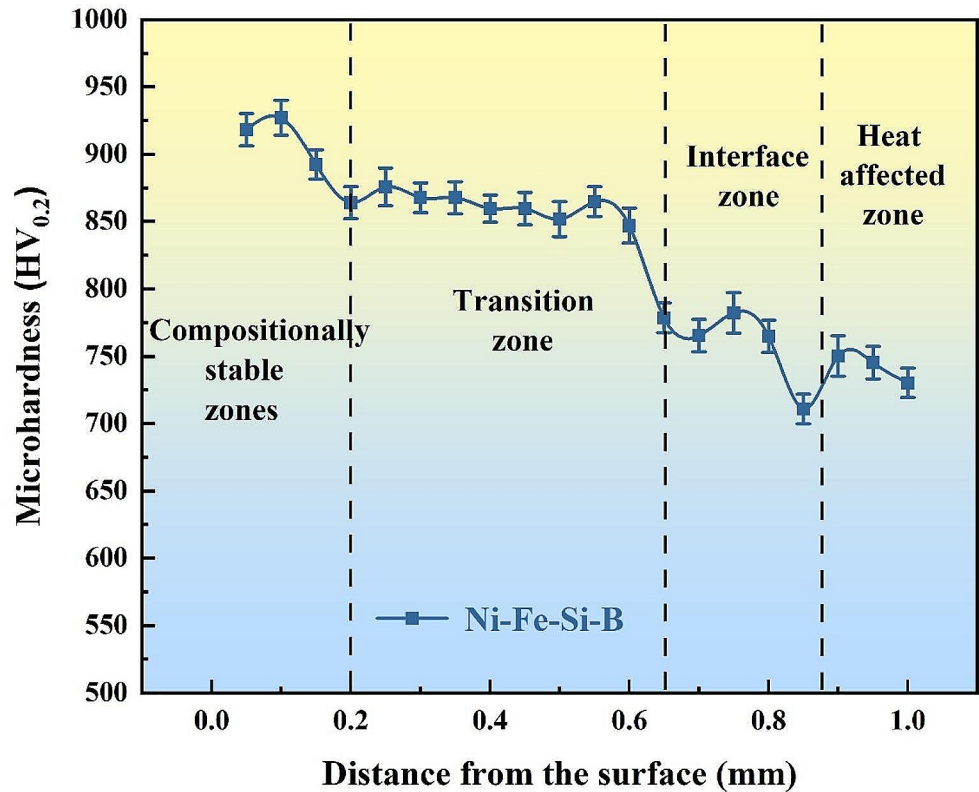**Fig. 6** Microhardness of the Ni–Fe–Si–B coating

Fig. 7 Friction and wear results of the H13 and Ni–Fe–Si–B coatings. (**a**) COF profiles. (**b**) wear volume loss

distance (m). The specific wear rate of the H13 substrate was 2.55×10^{-6} mm$^3 \cdot$N$^{-1} \cdot$m^{-1}, and the specific wear rate of the Ni–Fe–Si–B coating was 1.49×10^{-6} mm$^3 \cdot$N$^{-1} \cdot$m^{-1}. The wear resistance of the Ni–Fe–Si–B coatings was more than 1.71 times higher than that of the H13 substrate.

The macroscopic morphologies of the worn surfaces in Fig. 8 were analyzed. The comparable wear track of H13's 3D morphology may be shown in Fig. 8(a). The various hues signify various depths; the darker the blue, the deeper the

worn scar. Similar-colored lines indicate furrows. Obvious grooves appeared on the surface of the H13 steel substrate, indicating that the substrate experienced severe abrasive wear. The depths of the abrasion marks were 10.3 μm and 6.8 μm for the H13 steel and Ni-Fe-Si-B coatings, respectively. Macroscopically, the decrease in the area of the abrasion marks indicated that the true contact area between the abrasive ball and the test surface decreased, which fully demonstrated that the Ni-Fe-Si-B coating had an superior
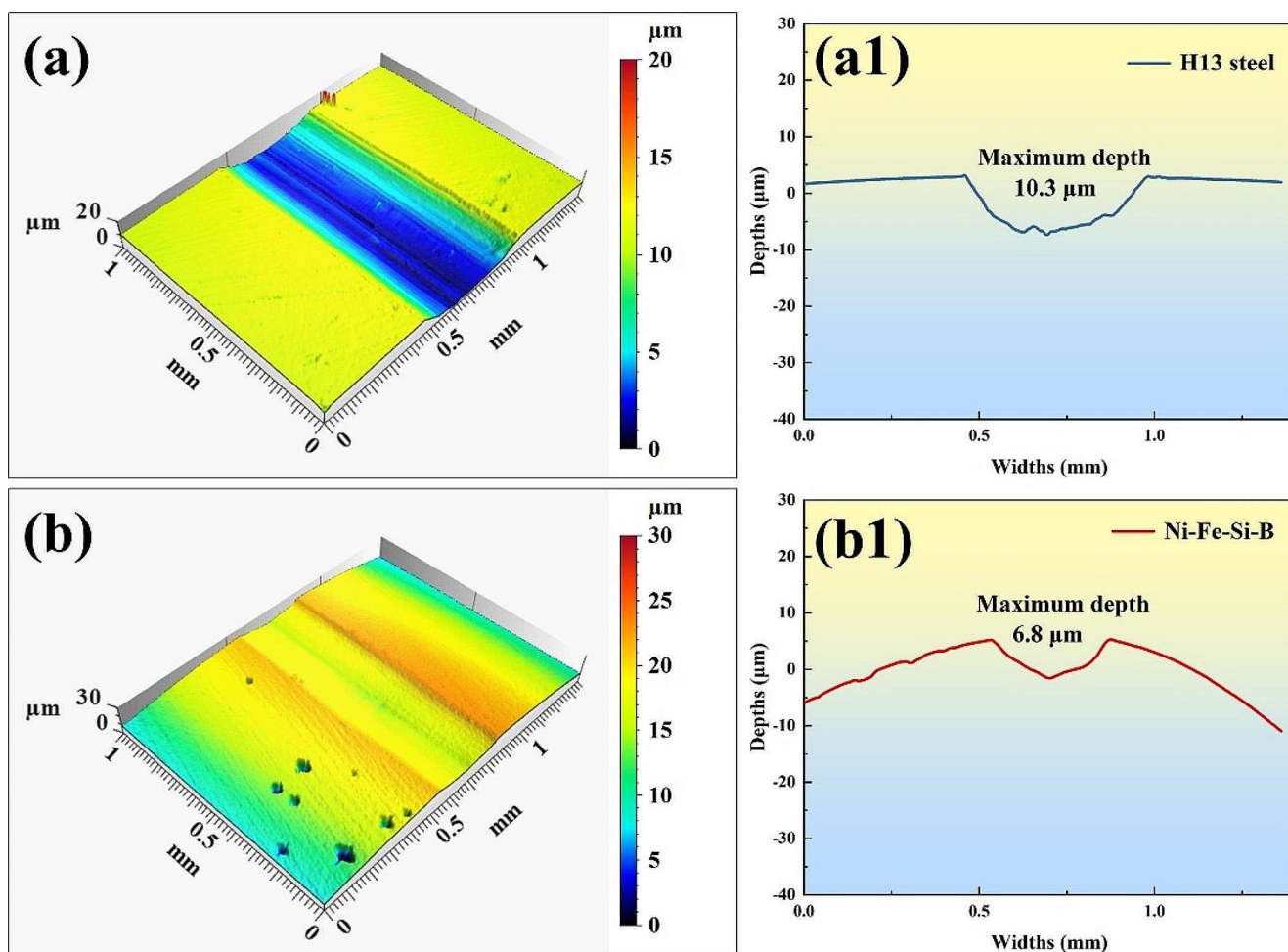
Fig. 8 Three-dimensional morphology of wear trajectory and cross-sectional curve of the wear scar: (**a**) and (**a1**) H13 steel; (**b**) and (**b1**) Ni–Fe–Si–B coating

wear resistance. The apparent accumulation of bumps on both sides of the wear marks suggests that during relative sliding, the material between the coating and the grinding ball tends to extrude along the sides rather than breaking up completely, which reflects the excellent plasticity of the coating, and, importantly, this property seems to correlate with the low wear rate of the material.

In order to analyze the wear mechanism of the H13 steel and the coating, SEM and EDS tests were carried out on the Al_2O_3 grinding balls, as shown in Fig. 9. As can be seen from the EDS in Table 2, wear areas have appeared on the surface of the grinding ball after rubbing with the H13 steel and a clear bonding layer has formed, which consists of oxides from the surface composition of the H13 steel and the grinding ball's own elements (Al and O), which suggests that adhesive wear accompanied by oxidation is the main wear mechanism of the H13 steel. From Fig. 9 (b), it can be found that a bonding layer also appeared on the surface of the Al_2O_3 grinding ball and the Ni-Fe-Si-B coating after friction. This bonding layer is mainly composed of Ni, Fe, Si

and O. During the sliding process, the softer $(Fe_{0.5}Ni_{0.5})_3Si$ flaked off to form fragments under the continuous tangential friction, and subsequently, the wear fragments were transferred and aggregated to the grinding balls [32].

To illustrate the underlying wear mechanisms related to the substrate and coatings, the wear surface morphology of the sample is shown in Fig. 10. Figure 10(a) shows the corresponding worn surface topography of H13. The wear surface of the matrix exhibits clear plastic deformation and deep furrows, indicating that the matrix has experienced severe abrasive wear. The oxides on the surface of H13 steel were tested by EDS as shown in Table 3. The surface morphology of H13 steel has white oxide and deep furrows, and the wear mechanism is mainly through oxidation and adhesive wear. At the beginning of the wear process, an oxide film formed on the surface of the H13 steel. With an increase in wear time, the oxide film fell off, resulting in direct contact between the grinding ball and the metal surface. Consequently, adhesive wear occurred, which was also proved by the fluctuation of the friction coefficient of H13
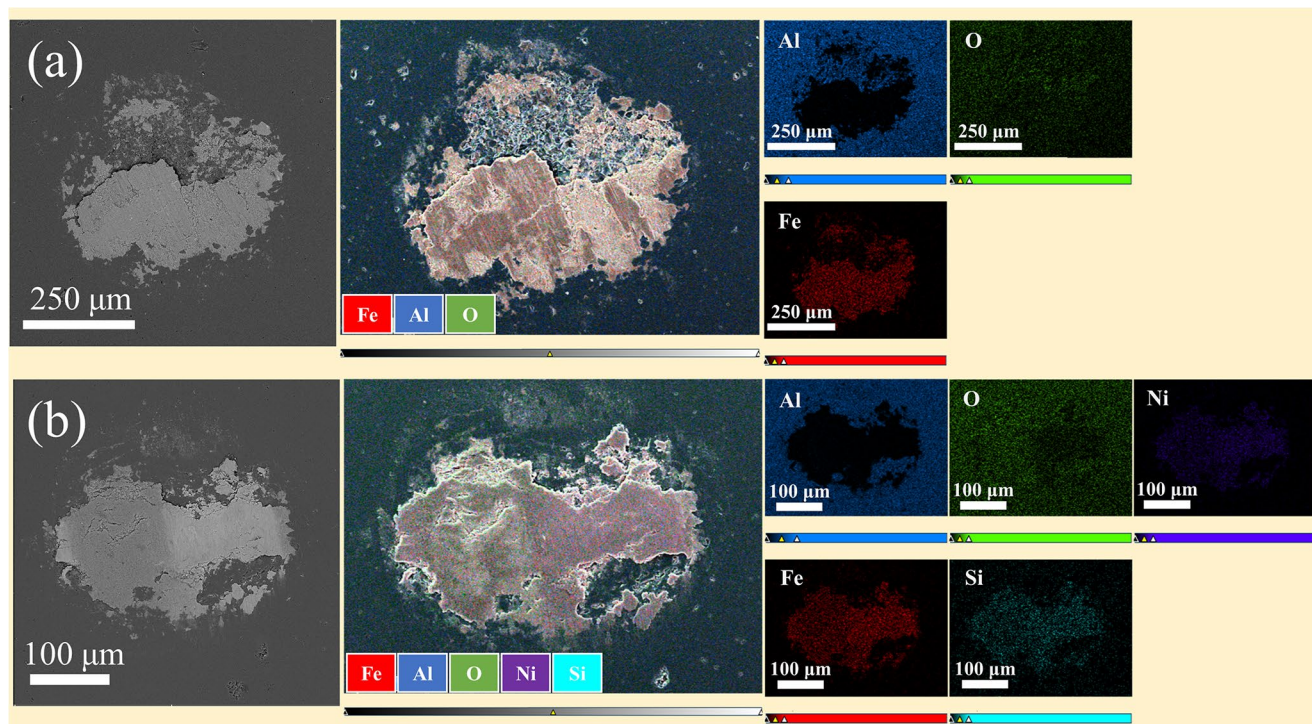
Fig. 9 SEM images of surface abrasions on Al₂O₃ balls: (**a**) H13 steel; (**b**) Ni-Fe-Si-B coating

Table 2 Chemical compositions (wt%) of positions marked in Fig. 9

Point	Ni	Fe	Si	B	Cr	Al	O
1		70.0			3.4	1.7	24.9
2	29.2	30.6	5.1			2.1	33.0
3						59.1	40.9

Fig. 10 Worn surface morphologies of (**a**) H13 steel and (**b**) Ni–Fe–Si–B coating
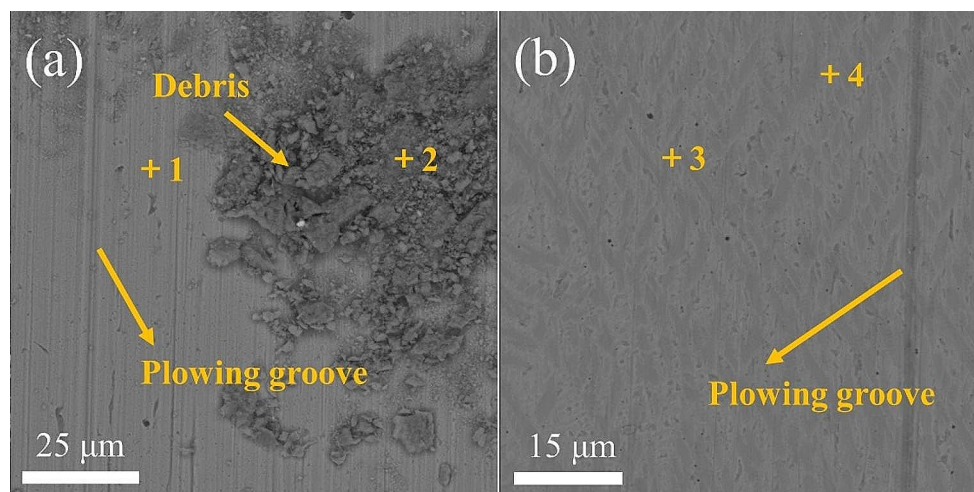
Table 3 Chemical compositions (wt%) of positions marked in Fig. 10

Point	Ni	Fe	Si	B	Cr	Al	O
1		91.9	2.9		5.2		
2		51.8	0.7		3.1	9.6	34.8
3	66.2	18.3	0.7	9.8			5
4	45.4	39.2	9.9	2.6			2.9

steel. Figure 10(b) shows the corresponding worn surface topography of the Ni–Fe–Si–B coatings. The surface of the worn coating is smooth with only a few grooves. The wear morphology of the coating was characterized by abrasive wear, and no cracks or spalling pits were observed.

In the process of friction and wear, the coupled interaction of the $(Fe_{0.5}Ni_{0.5})_3Si$, Fe_2B, $Ni_{31}Si_{12}$, and amorphous phase determines the wear resistance of the coating. The hard Fe_2B phase plays a supporting role in avoiding considerable abrasive wear, whereas the soft $(Fe_{0.5}Ni_{0.5})_3Si$ phase can prevent crack propagation [26, 33, 34]. Fe_2B is an intermetallic compound with exceptional hardness and wear resistance that was dispersed throughout the coating. Because to dispersion strengthening, Fe_2B has enhanced wear resistance [35, 36]. The solution strengthening of $(Fe_{0.5}Ni_{0.5})_3Si$ was useful for improving wear resistance. Furthermore, no long-range ordered microstructure or crystalline flaws such grain boundaries, dislocations, or precipitates were seen in the coating, indicating that the amorphous composite coating exhibits high wear resistance.

4 Conclusions

(1) A Ni–Fe–Si–B coating was prepared on the surface of H13 steel using laser-cladding technology. The coating that doesn't have any cracks show that the forming quality is good; a strong metallic bond is made between the coatings and the substrate.

(2) The coatings comprised three layers according to the microstructural analysis: the interface, transition, and compositionally stable zones. The Ni–Fe–Si–B coating was mainly composed of $(Fe_{0.5}Ni_{0.5})_3Si$, Fe_2B, Fe_2NiB, $Ni_{31}Si_{12}$, and an amorphous phase. Amorphous and crystalline phases coexisted in the coating, as shown by the XRD and TEM data, with an amorphous phase percentage of up to 57%. The analysis of the process by which complex phases of the organization form in composite coatings is emphasized.

(3) The surface exhibits the greatest hardness, measuring approximately 927.04 $HV_{0.2}$. In comparison with H13 steel, the wear resistance of the Ni–Fe–Si–B coating was more than 1.71 times higher than that of the H13 steel; thus, the coating exhibited high resistance to friction and wear. The wear mechanism of the Ni–Fe–Si–B coating was abrasive wear. The coupled interaction of $(Fe_{0.5}Ni_{0.5})_3Si$, Fe_2B and the amorphous phase determined the wear resistance of the coating.

Author Contributions Xuanhong Hao: Conceptualization, Validation, Investigation, Methodology, Writing – original draft. Hongxi Liu: Supervision, Funding acquisition, Project administration. Xiaowei Zhang: Supervision, Project administration. Yueyi Wang: Editing, Supervision. Chen Yang: Editing. Yaxia Liu: Editing. All authors read and approved the final manuscript.

Declarations

Competing interest The authors declare that they have no known competing financial interests or personal relationships that could have appeared to influence the work reported in this paper.

References

1. S.L. Wang, Z.Y. Zhang, Y.B. Gong, G.M. Nie, J. Alloys Compd. **728**, 1116–1123 (2017). https://doi.org/10.1016/j.jallcom.2017.08.251
2. X. Xie, C. Chen, Y. Xie, Z. Ren, E. Aubry, G. Ji, H. Liao, J. Alloys Compd. **749**, 523–533 (2018). https://doi.org/10.1016/j.jallcom.2018.03.306
3. G. Huang, L. Qu, Y. Lu, Y. Wang, H. Li, Z. Qin, X. Lu, Vacuum. **153**, 39–42 (2018). https://doi.org/10.1016/j.vacuum.2018.03.042
4. E. Williams, N. Lavery, J. Mater. Process. Technol. **247**, 73–91 (2017). https://doi.org/10.1016/j.jmatprotec.2017.03.034
5. Y. Li, X. Jia, W. Zhang, Y. Zhang, G. Xie, Z. Qiu, J. Luan, Z. Jiao, J. Mater. Sci. Technol. **65**, 171–181 (2021). https://doi.org/10.1016/j.jmst.2020.05.049
6. H. Zhang, C. Chen, Y. Fan, Y. Yang, L. Liu, R. Wei, T. Wang, W. Zhao, F. Li, J. Magn. Magn. Mater. **509**, 166875 (2020). https://doi.org/10.1016/j.jmmm.2020.166875
7. L. Shi, K. Yao, Mater. Design. **189**, 108511 (2020). https://doi.org/10.1016/j.matdes.2020.108511
8. H. Yang, Y. Liu, T. Zhang, H. Wang, B. Tang, J. Qiao, J. Mater. Sci. Technol. **30**(6), 576–583 (2014). https://doi.org/10.1016/j.jmst.2014.05.004
9. M. Aghasibeig, H. Fredriksson, Surf. Coat. Technol. **209**, 32–37 (2012). https://doi.org/10.1016/j.surfcoat.2012.08.013
10. S. Chen, R. Li, Q. Zheng, Z. Li, Mater. Trans. **57**(10), 1807–1810 (2016). https://doi.org/10.2320/matertrans.M2016189
11. J. Farmer, J.-S. Choi, C. Saw, J. Haslam, D. Day, P. Hailey, T. Lian, R. Rebak, J. Perepezko, J. Payer, D. Branagan, B. Beardsley, A. D'amato, L. Aprigliano, Metall. Mater. Trans. A **40**(6), 1289–1305 (2009). https://doi.org/10.1007/s11661-008-9779-8
12. K. Cui, Y. Zhang, Coatings. **13**(3), 635 (2023). https://doi.org/10.3390/coatings13030635
13. N. Aronhime, P. Ohodnicki, M.E. McHenry, Scr. Mater. **169**, 9–13 (2019). https://doi.org/10.1016/j.scriptamat.2019.05.003
14. Y. Geng, Z. Zhang, Z. Wang, Y. Wang, J. Qiang, C. Dong, H. Wang, O. Tegus, J. Non-Cryst Solids. **450**, 1–5 (2016). https://doi.org/10.1016/j.jnoncrysol.2016.07.032
15. E. Zaiser, X.Y. Zhou, A.M. Manzoni, S. Haas, U. Glatzel, X.P. Zhang, G.B. Thompson, W. Li, F. Vogel, Acta Mater. **195**, 327–340 (2020). https://doi.org/10.1016/j.actamat.2020.05.023
16. Y. Lu, G. Huang, Y. Wang, H. Li, Z. Qin, X. Lu, Mater. Lett. **210**, 46–50 (2018). https://doi.org/10.1016/j.matlet.2017.08.125
17. F. Shu, B. Zhang, T. Liu, S. Sui, Y. Liu, P. He, B. Liu, B. Xu, Surf. Coat. Technol. **358**, 667–675 (2019). https://doi.org/10.1016/j.surfcoat.2018.10.086

18. Z. Chang, W. Wang, Y. Ge, J. Zhou, Z. Cui, J. Alloys Compd. **747**, 401–407 (2018). https://doi.org/10.1016/j.jallcom.2018.02.296
19. P. Zhang, H. Yan, C. Yao, Z. Li, Z. Yu, P. Xu, Surf. Coat. Technol. **206**(6), 1229–1236 (2011). https://doi.org/10.1016/j.surfcoat.2011.08.039
20. J. Zhou, D. Kong, J. Alloys Compd. **795**, 416–425 (2019). https://doi.org/10.1016/j.jallcom.2019.05.012
21. J. Zhao, Q. Gao, H. Wang, F. Shu, H. Zhao, W. He, Z. Yu, J. Alloys Compd. **785**, 846–854 (2019). https://doi.org/10.1016/j.jallcom.2019.01.056
22. J. Lin, Z. Wang, J. Cheng, M. Kang, X. Fu, S. Hong, Results Phys. **12**, 597–602 (2019). https://doi.org/10.1016/j.rinp.2018.12.007
23. N. Simos, Z. Zhong, E. Dooryhee, S. Ghose, S. Gill, F. Camino, İ. Şavklıyıldız, E.K. Akdoğan, J. Nucl. Mater. **489**, 164–179 (2017). https://doi.org/10.1016/j.jnucmat.2017.03.030
24. K. Qi, Y. Yang, W. Liang, K. Jin, L. Xiong, Ceram. Int. **47**(20), 29463–29474 (2021). https://doi.org/10.1016/j.ceramint.2021.07.114
25. H. Lu, X. Zhang, J. Liu, S. Zhao, X. Lin, H. Li, Y. Hu, J. Alloys Compd. **925**, 166720 (2022). https://doi.org/10.1016/j.jallcom.2022.166720
26. Z. Peilei, L. Yunlong, Y. Hua, M. Kai, X. Peiquan, Y. Zhishui, C. Yingying, D. Min, Surf. Coat. Technol. **236**, 84–90 (2013). https://doi.org/10.1016/j.surfcoat.2013.09.032
27. S. Cao, J. Liang, J. Zhou, L. Wang, Surf. Interfaces. **21**, 100652 (2020). https://doi.org/10.1016/j.surfin.2020.100652
28. P. Zhang, M. Li, H. Yan, J. Chen, Z. Yu, X. Ye, J. Alloys Compd. **785**, 984–1000 (2019). https://doi.org/10.1016/j.jallcom.2019.01.191
29. H.X. Zhang, J.J. Dai, C.X. Sun, S.Y. Li, J. Mater. Process. Technol. **282**, 116671 (2020). https://doi.org/10.1016/j.jmatprotec.2020.116671
30. C. Deng, Y. Yi, M. Jiang, L. Hu, S. Zhou, Ceram. Int. **49**(20), 32885–32895 (2023). https://doi.org/10.1016/j.ceramint.2023.07.262
31. J.F. Archard, J. Appl. Phys. **24**(8), 981–988 (1953). https://doi.org/10.1063/1.1721448
32. Y. Wang, Y. Yang, H. Yang, M. Zhang, S. Ma, J. Qiao, Mater. Chem. Phys. **210**, 233–239 (2018). https://doi.org/10.1016/j.matchemphys.2017.05.029
33. Y. Li, H. Liang, Q. Nie, Z. Qi, D. Deng, H. Jiang, Z. Cao, Crystals. **10**(5), 352 (2020). https://doi.org/10.3390/cryst10050352
34. J. Cheng, B. Sun, Q. Liu, X. Liang, Surf. Coat. Technol. **307**, 728–734 (2016). https://doi.org/10.1016/j.surfcoat.2016.09.084
35. C. Wang, Z. Wu, X. Feng, Z. Li, Y. Gu, Y. Zhang, X. Tan, H. Xu, Intermetallics. **118**, 106689 (2020). https://doi.org/10.1016/j.intermet.2019.106689
36. Y. Wu, X. Liu, Z. Lu, M. Yang, X. Wang, H. Wang, S. Jiang, Sci. Sin. Phys. Mech. As. **50**(6), 067003 (2020). https://doi.org/10.1360/sspma-2019-0327